

## Article

# Two-Dimensional Flood Inundation Modeling in the Godavari River Basin, India—Insights on Model Output Uncertainty

Vimal Chandra Sharma \*  and Satish Kumar Regonda

Environmental and Water Resources Engineering, Department of Civil Engineering, Indian Institute of Technology Hyderabad, Kandi Village, Telangana 502285, India; satishr@ce.iith.ac.in

\* Correspondence: ce16resch01005@iith.ac.in

**Abstract:** Most flood inundation models do not come with an uncertainty analysis component chiefly because of the complexity associated with model calibration. Additionally, the fact that the models are both data- and compute-intensive, and since uncertainty results from multiple sources, adds another layer of complexity for model use. In the present study, flood inundation modeling was performed in the Godavari River Basin using the Hydrologic Engineering Center—River Analysis System 2D (HEC-RAS 2D) model. The model simulations were generated for six different scenarios that resulted from combinations of different geometric, hydraulic and hydrologic conditions. Thus, the resulted simulations account for multiple sources of uncertainty. The SRTM-30 m and MERIT-90 m Digital elevation Model (DEM), two sets of Manning’s roughness coefficient (Manning’s  $n$ ) and observed and estimated boundary conditions, were used to reflect geometric, hydraulic and hydrologic uncertainties, respectively. The HEC-RAS 2D model ran in an unsteady state mode for the abovementioned six scenarios for the selected three flood events that were observed in three different years, i.e., 1986, 2005 and 2015. The water surface elevation ( $H$ ) was compared in all scenarios as well as with the observed values at selected locations. In addition, ‘ $H$ ’ values were analyzed for two different structures of the computational model. The average correlation coefficient ( $r$ ) between the observed and simulated  $H$  values is greater than 0.85, and the highest  $r$ , i.e., 0.95, was observed for the combination of MERIT-90 m DEM and optimized (obtained via trial and error) Manning’s  $n$ . The analysis shows uncertainty in the river geometry information, and the results highlight the varying role of geometric, hydraulic and hydrologic conditions in the water surface elevation estimates. In addition to the role of the abovementioned, the study recommends a systematic model calibration and river junction modeling to understand the hydrodynamics upstream and downstream of the junction.

**Keywords:** flood inundation modeling; Godavari River; DEM; SRTM-30 m; MERIT-90 m; full-momentum equation; diffusion wave equation; Manning’s roughness coefficient; HEC-RAS 2D; hydrologic uncertainty; river junction



**Citation:** Sharma, V.C.; Regonda, S.K. Two-Dimensional Flood Inundation Modeling in the Godavari River Basin, India—Insights on Model Output Uncertainty. *Water* **2021**, *13*, 191. <https://doi.org/10.3390/w13020191>

Received: 12 November 2020

Accepted: 8 January 2021

Published: 14 January 2021

**Publisher’s Note:** MDPI stays neutral with regard to jurisdictional claims in published maps and institutional affiliations.



**Copyright:** © 2021 by the authors. Licensee MDPI, Basel, Switzerland. This article is an open access article distributed under the terms and conditions of the Creative Commons Attribution (CC BY) license (<https://creativecommons.org/licenses/by/4.0/>).

## 1. Introduction

Flooding is one of the natural hazards that is observed globally; however, flood events have different aspects and generating mechanisms, and localized geomorphological processes such as erosion and sediment deposition along the river play a key role in flood inundation, and consequently, flood impacts [1]. Flood inundation modeling, which typically consists of modeling of flow aspects due to the above complex processes, requires detailed information so that the models can run at the required scale [2]. With the advent of efficient numerical methods in combination with high-performance computing resources in recent times, flood inundation models have made a significant leap in their modeling capabilities, including their capability for producing reliable and accurate estimates of various flow aspects [3]. However, relatively, less research has been pursued in the context of uncertainties that associated with the model estimates [4–7]. A potential review on

the possibilities of flood modeling with different methods, advancements and sources of uncertainty was discussed by [8], while present and future directions are provided by [9]. Knowing that uncertainties in model estimates are unavoidable [10–12], and the increased perception about uncertainty and ensemble forecasts [13,14], in combination with enhanced activity in the recent decade in both the research and operational hydrologic realm [15–19], makes it clear that the uncertainty concept should be adopted in flood inundation modeling.

Hydraulic models with different capabilities, for example, 1D and 2D approaches [20], different numerical methods and a shock capturing scheme representing advanced hydrodynamics and parallel computation algorithms [21], are run in major river systems at finer [3,21–23] and coarser resolutions across the globe [24–26]. The model performance is analyzed with respect to the input, parameters and structure. A model's inputs for flood inundation mapping consist of floodplain geometry, land use, Manning's roughness coefficient, streamflow and water level at multiple locations. Note that uncertainties in measured as well as estimated values of the above vary at both spatial and temporal scales [27–31]. Among all, the model's geometry, particularly the elevation information, is treated as the primary source of uncertainty for the model flood inundation estimates [32–36]. In addition, the role of friction and conveyance in hydrodynamic modeling [37–39] and model structure related uncertainty [40,41] has been explored.

Hydrodynamic modeling in one and two dimensions (1D and 2D) is available for real-time flood forecasting [42]. However, the wide use of 1D models is followed by coupled 1D/2D or 2D models [10,42–47]. In recent times, 2D models have gained much attention with the evolution of finer resolution elevation models and land use data sets [10,48–55]. A comparison between 1D and 2D modeling highlighted the role of the model structure in flood inundation modeling [56].

Only a few studies addressed uncertainties in the flood inundation estimates, and many of them handled one source of uncertainty, i.e., uncertainties in flow inundation estimates are addressed with respect to the Manning's roughness [57–61], model structure [6,12] and initial and boundary conditions [29]. Additionally, uncertainty because of the limitations of governing equations to compute the frictional and bed slope has also been explored [62,63]. Very few studies successfully implemented the Generalized Likelihood Uncertainty Estimation (GLUE) framework [64] into the hydraulic models to determine the parameter sensitivity and associated uncertainty [65–67]. The uncertainty can arise from various aspects of inputs, including satellite-based estimates and rainfall-runoff model simulations [68,69]. The initial and boundary conditions consist of hydrological information, which can be estimated accounting for uncertainty via various advanced techniques, for example, copula-based bivariate or multivariate frequency analysis [70–73]. In addition, the uncertainty that comes from model structure simulating flow processes has not been studied in detail. This highlights the need for studies that calculate uncertainties from multiple sources in a study location so that influence of different types of uncertainties can be understood. In this context, this study calculates the model output at a location with varying sources of uncertainties, and then provides insights on the role of the sources of the uncertainties.

The Godavari River is the second longest river in India, and its drainage area, ~312,812 km<sup>2</sup>, lists the Godavari River Basin (GRB) as the third largest river basin in India [74]. The Godavari River receives large amounts of rainfall during the monsoon, which in association with climate change, for example, changes in rainfall amounts, duration and frequency [75–78], increases the flood likelihood along its major course. While no detailed studies have been carried out for flood inundation, flood inundation maps, for different flood events, each event from a year, has been calculated from satellite maps for Sabari River Basin, a sub-basin of the Godavari River Basin [79].

The present study considered a 240 km stretch along the major course of the river between the two gauge-discharge (GD) stations, Perur to Polavaram in the lower part of the Godavari River Basin (LGB), and a 35 km stretch on the Sabari River from Konta GD station,

the outlet of the Sabari sub-basin, to Kunavaram, where the river Sabari confluences with the Godavari River. The 35 km stretch on the Sabari River considered for the followings reasons, i.e., the Sabari River is the only major tributary that joins the Godavari on its 240 km stretch and its confluence at the river junction Kunavaram generates turbulence and forms backwaters on the Sabari River during very high flows [personal communication with the Central Water Commission (CWC) of India personnel] [80].

The research presented in this paper aims to provide insights on the uncertainty in the model output from six scenarios, which are formed with Shuttle Radar Topographic Mission (SRTM)—30 m—and Multi Error Removed Improved Terrain (MERIT)—90 m digital elevation models (DEMs), initial and optimized Manning’s  $n$  values and observed and estimated flow boundary conditions. In this study, DEM based cross-sections compared with the measured cross-section. For the six scenarios, we analyzed the error in the water surface elevation at each computational cell and compared stage hydrographs of selected events for locations of upstream and downstream of the river junction. Also, the calculations were done for different model structures. The results obtained from the above analysis assisted in providing the model output uncertainty.

## 2. Materials and Methods

### 2.1. Study Area

The Godavari River flows for 1465 km from west to east and drains an area of  $\sim 312,812 \text{ km}^2$ , which is about 10% of the total geographical area of India. The Godavari River Basin (GRB) is categorized into upper, middle and lower river basins, and the Lower Godavari Basin (LGB) occupies nearly 28% of the area of the GRB. Two stretches of rivers of 240 km and 35 km length on the Godavari River and Sabari River, respectively, were considered for this study, and these vary in their topographic and hydrologic aspects. The daily average flows (peak water surface elevations) are  $465 \text{ m}^3/\text{s}$  (49.91 m),  $2204 \text{ m}^3/\text{s}$  (84.42 m) and  $2725 \text{ m}^3/\text{s}$  (28.02 m) at locations Konta (upstream of the Sabari River stretch), Perur (upstream of the Godavari River stretch) and Polavaram (downstream of the Godavari River stretch), respectively, for the period 1966–2015. The elevation at the Perur and Polavaram GD stations is approximately 75 m and 19 m, respectively, and the average slope of the channel is approximately 0.3%. The elevation at Konta GD station on the Sabari River is about 36 m, and the average slope of the river up to the outlet is about 0.2%. Figure 1 shows the location of the study area.

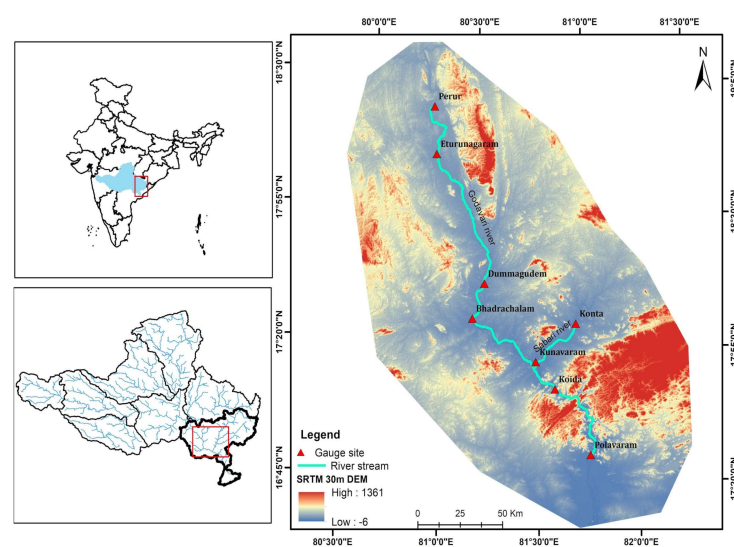


**Figure 1.** Location map of the study site showing Godavari River and Sabari River in the lower Godavari River Basin, India. Gauge stations, including the Central Water Commission (CWC) measurements of the streamflow and level, are shown in triangles.

## 2.2. Data

Two digital elevation models (DEMs), i.e., the Multi Error Removed Improved Terrain—90 m (MERIT-90 m) [81] and the Shuttle Radar Topographic Mission—30 m (SRTM-30 m) [82], were used to develop the two-dimensional geometrical mesh of the study area. Land use and land cover (LULC) data with a spatial resolution of 100 m for the years 1985 and 2005 were obtained from the Oak Ridge National Laboratory Distributed Active Archive Center (ORNL DAAC), whereas LULC data with a spatial resolution of 56 m for the year 2011 were obtained from the Indian Space Research Organization (ISRO)'s geoportal Bhuvan [83]. The study area can be categorized into 9 and 12 different land use and land cover classes for 1985 and 2005, and 2011, respectively, based on their land use. Manning's  $n$  values were obtained from both the National Land Cover Dataset (NLCD) [84] and the HEC-RAS manual [85]. The observed data of hydraulic variables, such as maximum velocity ( $V$ ), wetted perimeter ( $P$ ), Manning's  $n$  and bottom frictional slope ( $S_0$ ), were obtained for each event on a daily time scale from the Krishna and Godavari Board Organization (KGBO), Hyderabad, India. The flow hydrographs at Perur and Konta were used as upstream boundary conditions, and the stage hydrograph at Polavaram was used as a downstream boundary condition for the HEC-RAS 2D model. For the Konta GD location, both the observed and estimated flow hydrographs were considered. The estimated streamflows were obtained from a calibrated hydrologic model, i.e., the Hydrologic Engineering Center—Hydrologic Modeling System (HEC-HMS), in a semi-distributed mode for the Sabari River Basin. We considered three large flood events, of which each event comes from a separate year, and the characteristics of the flood events are shown in the Table 1. Note that the start and end of the event is subjective, and the dates were selected after a detailed analysis of the flow hydrographs of the events.

**Table 1.** Duration of the event ( $t$ ), Peak flow ( $Q_p$ ), peak water surface elevation ( $H_p$ ) and time to peak ( $T_p$ ) for the selected three flood events (E1, E2 and E3) at a boundary condition gauge location.  $Q^*_p$  reflects the estimated values from the calibrated HEC-HMS model.

Event	Perur				Konta			Polavaram		
	$t$ (Days)	$Q_p$ ( $m^3/s$ )	$H_p$ (m)	$T_p$ (Date)	$Q_p$ ( $m^3/s$ )	$Q^*_p$ ( $m^3/s$ )	$T_p$ (Date)	$Q_p$ ( $m^3/s$ )	$H_p$ (m)	$T_p$ (Date)
22-07-1986 to 02-09-1986 (E1)	42	62,889.13	87.42	15-08-1986	20,187.04	10,400.1	17-08-1986	57,310.57	28.017	16-08-1986
11-09-2005 to 28-09-2005 (E2)	18	24,436.1	81.13	18-09-2005	8853.78	9224.6	20-09-2005	43,703.04	25.897	21-09-2005
10-06-2015 to 30-06-2015 (E3)	21	22,779.00	80.08	22-06-2015	7468	9107.40	21-06-2015	22.82	22433.00	23-06-2015

## 2.3. HEC-RAS 2D Model Setup

### 2.3.1. Developing 2D Flow Area

An unstructured computational mesh of grid size 250 m  $\times$  250 m was developed for the flow area (Figure 2). The 2D flow area consists of 52,241 computational cells, of which many cells, i.e., ~95%, are of 250 m resolution; the maximum, minimum and average area of all the cells is approximately 0.14 km<sup>2</sup>, 0.009 km<sup>2</sup> and 0.062 km<sup>2</sup>, respectively. The 2D area break lines are applied to the cells of high elevation zones over which water does not flow to avoid a numerical error; a high elevation zone can be a structure or an object that acts as a barrier to the flow or that controls the flow direction. The boundary condition lines are drawn at Perur and Polavaram on the Godavari River and at Konta on the Sabari River.

### 2.3.2. Manning's $n$ Values

Manning's roughness coefficients (Manning's  $n$ ) for each grid cell of the flow area are assigned based on the land use classes of the corresponding grid cell. The LULC maps corresponding to the years 1985, 2005 and 2011 were used for three events, i.e., 1986, 2005 and 2015, respectively. Note that the LULC maps, which require significant effort, are developed for every 5 or 10 years, assuming that the LULC data do not change drastically

in a short period of the time except for in a few situations, e.g., deforestation and conversion of agricultural land into non-agricultural land. Therefore, the existing LULC maps of the years 1985 and 2011 are used for 1986 and 2015, respectively. The study area is represented with 09-, 09- and 12-land use classes for the years 1985, 2005 and 2011, respectively. LULC maps of relatively coarser resolution were downscaled to a DEM resolution for the years 1985 and 2005, whereas the LULC maps with relatively finer resolution aggregated to a DEM resolution for the year 2011. As per the land use classes, Manning's  $n$  values were obtained from two different sources, i.e., NLCD and HEC-RAS user's manual; then, Manning's  $n$ -values for the 250 m grid cell is assigned based on the average of Manning's  $n$ -values of grids of the DEM. – NLCD based- and optimized- Manning's  $n$  values were derived using HEC-RAS user manual-based values as initial values, shown in the top and bottom rows of Figure 3, respectively, for three different events.

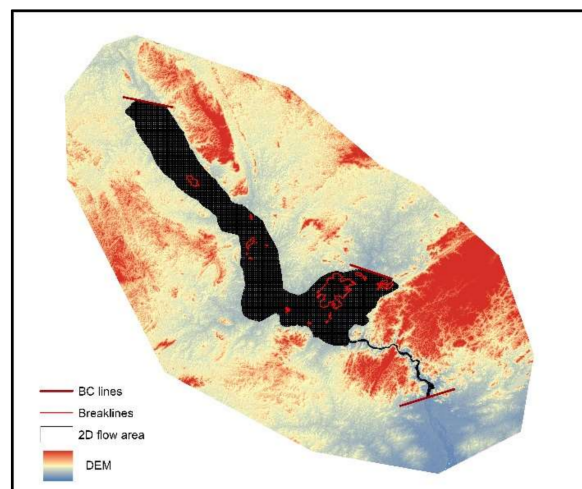


**Figure 2.** Two-dimensional unstructured computational mesh generated with a cell size of 250 m. Boundary conditions were applied at three locations (denoted with linear sections), and areas within the break lines (red colored closed curves) denote the infected flow areas.

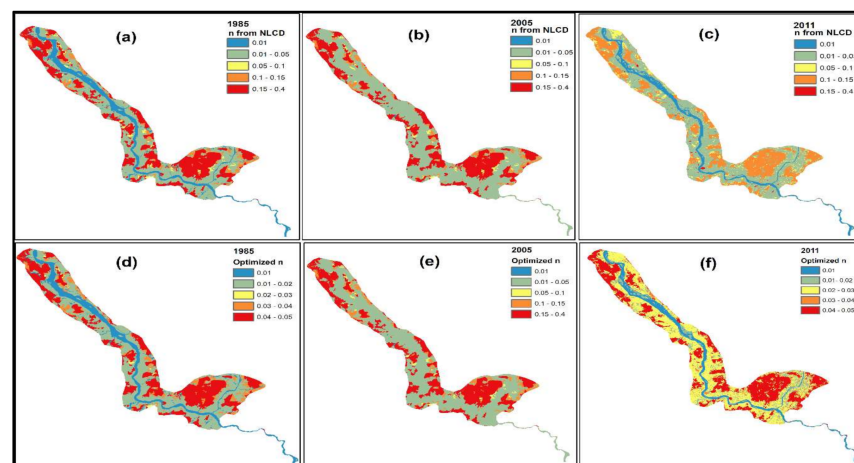


**Figure 3.** Distribution of Manning's roughness coefficient ( $n$ ) within the flow area. The top row, i.e., (a–c) corresponds to the initial values calculated using the land use classes from National Land Cover Dataset (NLCD) database. The bottom row, i.e., (d–f) corresponds to the optimized Manning's  $n$  values that are derived using HEC-RAS user manual values as initial values. Column-wise, figures from left to right correspond to the years 1985, 2005 and 2011, respectively.

### 2.3.3. Governing Equations

The 2D St. Venant equations, i.e., both the continuity and momentum equations were solved to estimate various flow aspects of unsteady flow in the river. The equations are given below.

Continuity equation:

$$\frac{\partial H}{\partial t} + \frac{\partial(hu)}{\partial x} + \frac{\partial(hv)}{\partial y} + q = 0 \quad (1)$$

where  $H$  is the water surface elevation (m),  $t$  is the time (s),  $h$  is the water depth in the cross-section (m),  $u$  and  $v$  are the velocity components (m/s) in the  $x$ - and  $y$ -directions, respectively, and  $q$  is the source or sink flux (m/s).

Momentum conservation equation:

$$\frac{\partial u}{\partial t} + u \frac{\partial u}{\partial x} + v \frac{\partial u}{\partial y} = -g \frac{\partial H}{\partial x} + v_t \left( \frac{\partial^2 u}{\partial x^2} + \frac{\partial^2 u}{\partial y^2} \right) - C_f u + f v \quad (2)$$

$$\frac{\partial v}{\partial t} + u \frac{\partial v}{\partial x} + v \frac{\partial v}{\partial y} = -g \frac{\partial H}{\partial y} + v_t \left( \frac{\partial^2 v}{\partial x^2} + \frac{\partial^2 v}{\partial y^2} \right) - C_f v + f u \quad (3)$$

where Equations (2) and (3) represents the conservation of momentum in the Cartesian coordinates [85],  $g$  is the acceleration due to gravity,  $v_t$  is the horizontal viscosity coefficient,  $C_f$  is the bottom friction and  $f$  is the Coriolis parameter. Parameters of the right side of the equations,  $v_t$  and  $C_f$ , can be estimated using the equations below:

$$v_t = Dhu^* \quad (4)$$

where  $D$  is a non-dimensional empirical constant and has a range from 0.33 to 0.77 [86]. The value 0.33 adopted in this study, and the value corresponds to moderate transversal mixing of turbulence for gentle meanders with moderate surface irregularities; 'h' is water depth at the cross-section and  $u_*$  is the shear velocity is given by:

$$u_* = \sqrt{gRS} \quad (5)$$

$$S = \left( \frac{|V| n}{1.49R^{0.006}} \right)^2 \quad (6)$$

$$c_f = \frac{n^2 g |V|}{R^{4/3}} \quad (7)$$

where  $g$  is the acceleration due to gravity,  $R$  is the hydraulic radius (m),  $S$  is the energy grade line (EGL) slope,  $|V|$  is the magnitude of the velocity vector (m/s) and  $n$  is Manning's roughness coefficient ( $s/m^{1/3}$ ).

Model stability condition:

The Courant Friedrichs Lewy (CFL) condition [87] was used to maintain the model stability:

$$C = \frac{V_w \Delta T}{\Delta X} \leq 1 \text{ or } \Delta T \leq \frac{\Delta X}{V_w} \quad (8)$$

where  $C$  is the Courant number,  $V_w$  is the wave speed (m/s),  $\Delta T$  is the numerical computation time interval (or time step) (minutes) and  $\Delta X$  is the distance interval (m). In the above equation,  $\Delta T$  was used to estimate the wave velocity and the courant number. Values of 'C' provide information on the convergence of the numerical solution and model stability. The  $C$  values greater than 3 and 5 for the full-momentum equation (FME) and diffusion wave equation (DWE), respectively, suggest that the model is unstable. Therefore, the selection of  $\Delta T$  is an important aspect for CFL condition. Initial values for  $\Delta T$  are assigned as 10 min. The value of  $\Delta X$  is 250 m.

Coriolis force effect:

The Coriolis force acts on the motion of all objects that on earth, which rotates around its own axis. Note that the vertical component of the Coriolis force is ignored, and the horizontal component of the force is proportional to the Coriolis parameter ( $f$ ). The Coriolis parameter,  $f$ , is calculated as below:

$$f = 2\omega \sin\varphi \quad (9)$$

where  $\omega = 0.00007292115855306587/s$ , which is the sidereal angular velocity [86] of the earth, and  $\varphi$  is the latitude, for which a value of  $17^\circ$  is considered.

#### 2.3.4. Model Parameters

The HEC-RAS 2D model needs to be supplied a set of 12 parameters, including the parameters that are mentioned in the above equations. While values of many parameters are initially assigned to a value based on the expertise or guidance such as the HEC-RAS user manual, they need to be modified so that estimated values are in agreement with observed stage values. Horizontal viscosity coefficient,  $\nu_t$ , is computed assuming a D value of 0.33, and the EGL slope is calculated separately for the three boundary condition locations and for the three different events using Equations (4) and (6). The EGL slope was computed as 0.000321538, 0.000226667 and 0.000192592 at Perur and 0.000156154, 0.000180769 and 0.000180769 at Konda for E1, E2 and E3, respectively. The initial conditions regarding the time for the model simulations are 3 h, 2.5 h and 2 h for E1, E2 and E3, respectively. The values of  $V_w$ , a parameter in the courant stability condition, are 2.33 m/s, 1.55 m/s and 2.1 m/s for E1, E2 and E3, respectively.  $\Delta T$ , a numerical computation time interval, varied from 10 min to 1 min. The implicit weighting factor ( $\theta$ ) corresponds to weights of the spatial derivatives at current and previous time steps, and the value of  $\theta$  varied from 0.6 to 1 to achieve the convergence to higher values of C. Note that values of various parameters were the same for all the three events.

#### 2.3.5. Model Simulations

The model ran for six different scenarios that resulted from two different DEM sources, two sets of Manning's  $n$  and two sets of boundary conditions. The scenario S1 (S2) consists of SRTM-30 m DEM, with NLCD-based (optimized) Manning's  $n$  and observed values as boundary conditions. The scenario M1 (M2) consists of MERIT-90 m DEM, with NLCD-based (optimized) Manning's  $n$  and observed values as boundary conditions. The scenario F1 (F2) consists of SRTM-30 m (MERIT-90 m) DEM, with optimized Manning's  $n$  and observed values on the Godavari River and estimated values on the Sabari River as boundary conditions. All simulations were performed on a daily time interval. In addition, simulations were generated employing model of different structures, i.e., the dynamic wave model and diffusion wave model. The momentum equation of the St. Venant equation corresponds to the dynamic wave model is labeled as the full momentum equation (FME). Removal of the local and convective acceleration terms including advection and viscous terms from the FME corresponds to the diffusion wave model and the new form labeled as the diffusion wave equation (DWE). The water surface elevation (H) time series for each grid cells of the flow area and inundation boundary (IB) for the event E2 are generated. The model calibration was done by optimizing the implicit weighting factor ( $\theta$ ), time step ( $\Delta T$ ) and Manning's  $n$  in a trial-and-error mode so that simulations and observed water surface elevation (H) are in close agreement at the selected three locations, i.e., Dummugudem, Bhadrachalam and Koida on the Godavari River.

#### 2.3.6. Model Performance

The model performance was assessed by comparing the observed and simulated water surface elevations (H) at specific locations for different events as mentioned below (Table 2), i.e., Dummugudem and Koida for E1 and E2, and Bhadrachalam for E3. The performance metrics consist of the correlation coefficient ( $r$ ), Index of agreement ( $d$ ), Mean

Absolute Error (MAE), Root Mean Squared Error (RMSE), Percentage Bias (PBIAS) [88] and Kling-Gupta Efficiency (KGE) [89].

**Table 2.** Performance metrics used for the model assessment.

Metric	Equation	Range
Correlation coefficient, r	$\frac{\sum_{i=1}^N (O_i - \bar{O})(P_i - \bar{P})}{\sqrt{\sum_{i=1}^N (O_i - \bar{O})^2 (P_i - \bar{P})^2}}$	-1 to 1
Index of agreement, d	$1 - \frac{\sum_{i=1}^N (O_i - P_i)^2}{\sum_{i=1}^N ( P_i - \bar{O}  +  O_i - \bar{O} )^2}$	0 to 1
Mean Absolute Error, MAE	$N^{-1} \sum_{i=1}^N  O_i - P_i $	0 to $\infty$
Root Mean Squared Error, RMSE	$\sqrt{\frac{\sum_{i=1}^N (O_i - P_i)^2}{N}}$	0 to $\infty$
Percent bias, PBIAS	$\frac{\sum_{i=1}^N (O_i - P_i)}{\sum_{i=1}^N O_i} \times 100$	$-\infty$ to $\infty$
Kling-Gupta Efficiency, KGE	$\frac{1 - \sqrt{(r - 1)^2 + (\alpha - 1)^2 + (\beta - 1)^2}}{1}$	$-\infty$ to 1

In Table 2, N indicates the number of observations or the duration of the event, O and P are the observed and simulated values,  $\bar{O}$  and  $\bar{P}$  correspond to average observed and simulated values, r is the correlation coefficient,  $\alpha$  is a measure of relative variability in the simulated and observed values and  $\beta$  is the ratio of  $\bar{P}$  and  $\bar{O}$ ; the square root term in the KGE equation denotes Euclidian distance (ED) from the ideal point.

### 3. Results

#### 3.1. Comparison of DEMs

The MERIT-90 m and SRTM-30 m DEMs are used to extract elevations, which are used in developing the 2D geometry for the study area. The weighted average of the elevations of the DEM grid cells corresponding to a HEC-RAS computational grid cell are calculated and the elevations from these two sources are compared for all the HEC-RAS computational grid cells (Figure 4a). While the scatter plot of these elevation values (Figure 4a) suggests a strong linear agreement (correlation of 0.99) among the elevations of the two sources, the histogram of the differences in elevation suggest that the elevations differ by as much as 30 m for a few grid cells, while a significant number of cells show a difference of 5 m or more (Figure 4b).

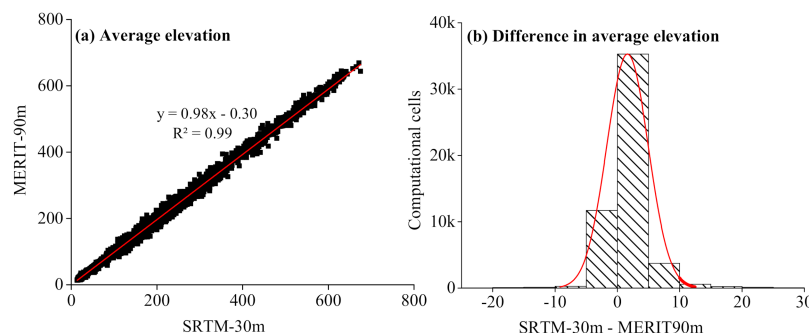


**Figure 4.** (a) Scatter plot of the weighted average elevation of grid cells derived from SRTM-30 m and MERIT-90 m DEMs and (b) histograms of differences in weighted average elevations of the cells based on SRTM-30 m and MERIT-90 m DEMs.

The cross-section plot of the two DEMs suggests differences in elevations as high as 5 m. As compared to the Bhadrachalam (Figure 5c), the cross-section plot of Koida (Figure 5d) highlights relatively low agreement between the two DEMs and the measured cross-sections. Note that the river at Bhadrachalam is wider, ~1.4 km in length, while elevations range from 32 to 50 m; the river at Koida is ~0.8 km and elevations range from

5 m to 40 m during 1986 and 8 m to 41 m during 2005. However, changes between the two years at Koida are observed. Connectivity between the circles was missing at a few places due to no elevation or station values for the measured as well as DEM-based cross-section profiles. Large deviations in SRTM-30 m-derived elevations were related to its relatively finer resolution.

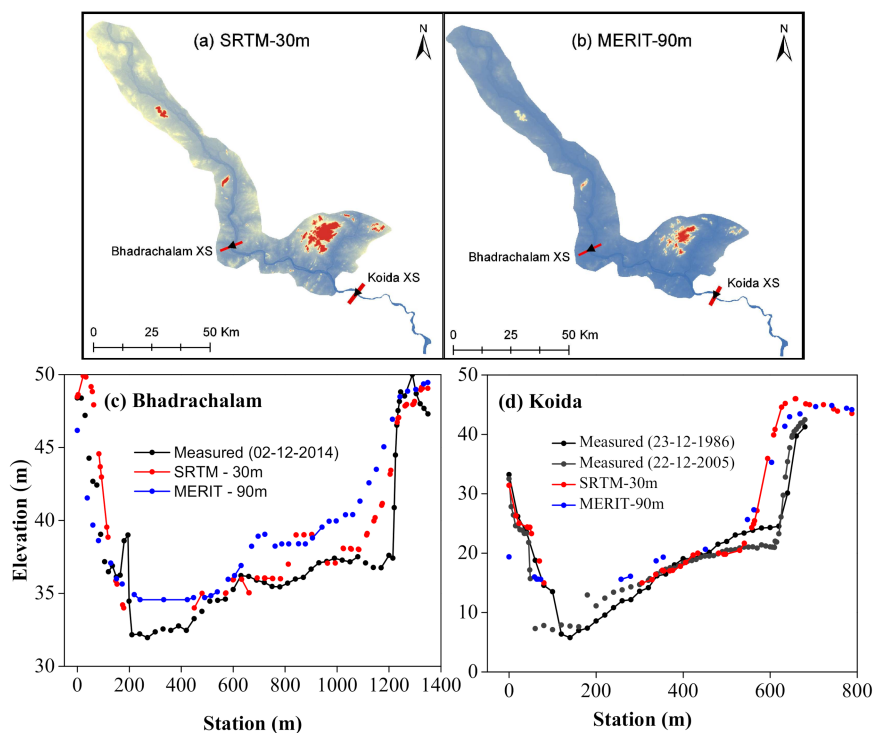


**Figure 5.** Comparison of cross-section derived from (a) SRTM-30 m and (b) MERIT-90 m and DEM at Bhadrachalam and Koida. The plots (c) and (d) show the cross-sectional elevation profiles at Bhadrachalam and Koida with the measured cross-section, respectively. A significant contraction in the river channel at Koida can be seen.

### 3.2. Model Calibration

The gridded Manning's  $n$  values, extracted from NLCD, exhibited a decreased pattern for three events in a chronological order (Figure 3a–c). The Manning's  $n$  values for the event in the year in 1986 are high, followed by the events in the years 2015 and 2005. The river in Figure 4b is not visible due to the date of the satellite image, which might have been taken during the river's dry season. On the other hand, optimized Manning's  $n$  values suggest relatively increased roughness values for the events in chronological order (Figure 3d–f) and decreased roughness values as compared to the NLCD-based values. The highest recorded flood event, i.e., the flood event in 1986, has optimized Manning's  $n$  values, ranging from 0.01 to 0.05 (Figure 3d). Relatively decreased roughness values with respect to the NLCD values might be because of the increased flows in the flow area (Figure 3a,d).

The model found to be stable for values of  $\Delta T$  are 1-, 1- and 2-min for E1, E3 and E2 events, respectively. Figure 6 shows the number of computational grid cells for different values of implicit weighting factor ( $\theta$ ) for the M2 scenario of E1, and it assists in understanding the effect of  $\theta$  on the model stability. The computational cells are the total number of grid cells minus the cells with an error below the specified threshold. These cells varied at 423, 390, 400, 480 and 553 for the theta values from 0.6 to 1 at an interval of 0.1. An increase in values  $\theta$  first resulted in a decreased ( $\theta$  from 0.6 to 0.7) and increased ( $\theta$  from 0.8 to 1) number of computational cells, which means the error in each cell decreased below the specified threshold in the case of  $\theta$  at 0.6 and 0.7 and increased in the remaining cases. Approximately, 24- and 10 computational cells with solution converged at the Courant

number 3 and 4, respectively. For the values of  $\theta = 0.6$  and  $0.7$ , approximately 5 and less than 10 cells converged respectively, with a solution. Convergence of the solution for the number of computational cells with the Courant number 2 increased linearly from  $\theta$ , 0.6 to 1. In addition, the cells correspond to C4, which refers to that the non-convergence of the model solution decreased in the case of  $\theta = 1$ ; the value of  $\theta = 1$  yielded a stable model, whereas  $\theta = 0.6$  also exhibited similar stability with more values converged at 1. The scenario with  $\theta = 0.6$  yield relatively more number of computational cells with acceptable error as compared to  $\theta = 1$ . However, the scenario is unstable due to the convergence of the solution with C4.

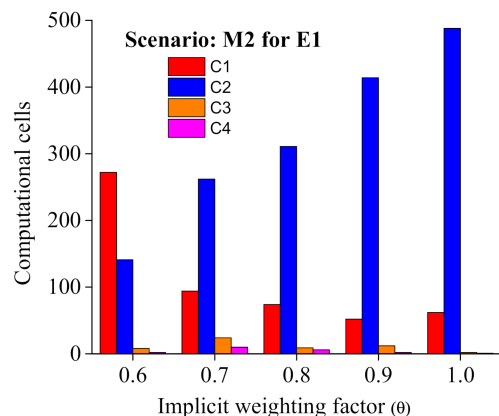


**Figure 6.** Optimization of  $\theta$  of the test case for the event E1 when MERIT-90 m used (M2 scenario). Here, C1, C2, C3 and C4 correspond to the solutions that converged with the Courant number 1, 2, 3 and 4, respectively, for the simulations obtained by using the full-momentum equation (FME).

### 3.3. Analysis of $H_{Error}$

The water surface elevation tolerance is set to its default values, i.e., 0.003 m, after which the error in water surface elevation ( $H_{Error}$ ), i.e., the difference between the computed value and assumed value, for each computational cell is calculated, which is then pooled for all computational cells and plotted in a boxplot (Figure 7). The plots are developed for all six scenarios and for each of the three events, and repeated for all three events.

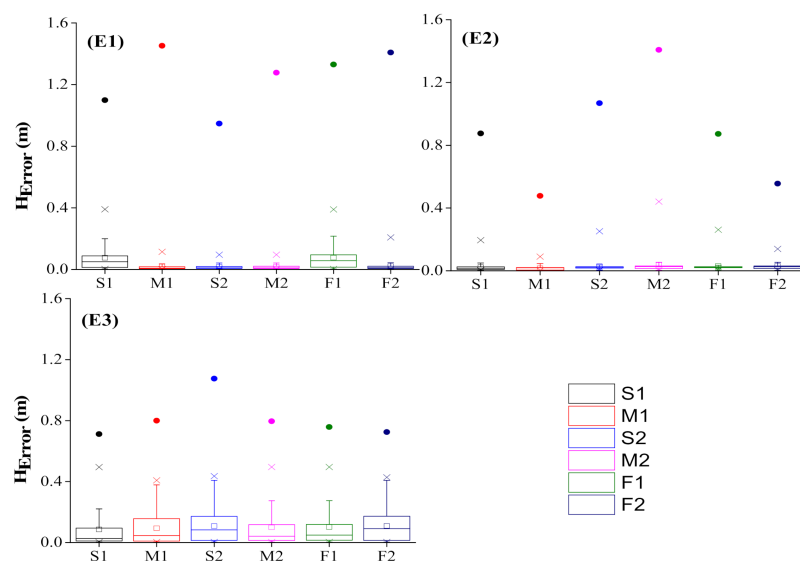


**Figure 7.** Boxplots of error in the estimated water surface elevation ( $H_{Error}$ ) at each computational cell for the six scenarios for the three events, E1, E2 and E3.

Small  $H_{\text{Error}}$  values ( $\sim < 0.1$  m) were observed for most of the cells (only two outside values were observed) for the M1, S2, M2 and F2 for (E1) and (E2) events. Relatively higher  $H_{\text{Error}}$  values were observed for S1 and M1 scenarios as compared to rest of the scenarios (median of  $H_{\text{Error}}$  is 0.05 m). Boxplots of smaller length and without a clear median suggests smaller and left-skewed  $H_{\text{Error}}$  values for E2 as compared to E1. The values are smaller for E1 and E2, and relatively higher for E3, for all scenarios. Nevertheless,  $H_{\text{Error}}$  for 75% of the cells is well below 0.2 m, and the upper whisker, which corresponds to  $\sim 99.5$  percentile, is below 0.4 m. The largest errors (outsiders of the boxplots, which correspond to less than 1% of the cells) vary with each configuration and event, and the values are smaller for event E2 as compared to E1 and E3.

MERIT-90 m DEM exhibited smaller  $H_{\text{Error}}$  values as compared to the SRTM-30 m DEM, and the relatively large error of the SRTM-30 m can be attributed to its finer resolution and large variability in the vales (Figure 2). The scenario with optimized Manning's n values and observed boundary conditions yield small  $H_{\text{Error}}$  values for both DEMs (S2 and M2). The configuration that includes SRTM-30 m DEM and either NLCD-based Manning's n values or estimated flows yield slightly higher  $H_{\text{Error}}$  values as compared to the other scenarios. The results suggest that the scenario of MERIT-90 m optimized Manning's n values and observed flows (M2) for better performance in terms of  $H_{\text{Error}}$ ; nevertheless, MERIT-90 m relatively decreased the performance observed for E3 as compared to the E1 and E2. Thus, the boxplots allow commenting on better performance across the study area; however, it is important to see in detail the values at a particular location. In this regard, to understand the model error with respect to time at a particular location space, stage hydrographs of simulated and observed values were developed.

#### 3.4. Comparison of Stage Hydrographs

Both observed and estimated stage hydrographs were compared for locations Dummugudem and Koida for E1 and E2, and for Bhadrachalam for E3. Figure 8 has five plots, of which each plot corresponds to a location and an event. Observed and estimated stage values from different scenario are denoted in different colors. Estimated stage hydrographs from all scenarios suggest realistic simulated hydrographs for all events. Nevertheless, overestimated stage values were observed for two events, E1 and E2, at both locations, Dummugudem and Koida, for all scenarios except for four at Dummugudem for E2; these four scenarios consist of optimized Manning's n values but differ in other sources of uncertainty. Irrespective of whether stages were over- or underestimated, the estimated values exhibited a systematic bias for the entire flood event, whereas the performance of event E3 differs slightly, i.e., under- and overestimated values can be observed on the rising and falling limb, respectively. Additionally, it is observed that the scenario with NLCD-based Manning's n values produced hydrographs of higher magnitude as compared to scenarios with optimized Manning's n values.

#### 3.5. Comparison of Flood Inundation Maps for the Event E2

Map of inundation boundary (IB) generated for all the six scenarios, for 22 September 2005, and compared with the flood extent estimated from the RADARSAT-1 imagery shown in the [67] for a downstream stretch of the Sabari River. Figure 9 shows maps of IB obtained from this study for six scenarios. While the maps of IB from all scenarios appear to be not deviating significantly, closer look of the same suggests the contradictory. High- and low- areas of inundation observed for scenarios that use NLCD-based Manning's n values and combination of SRTM-30 m and optimized Manning's n values, respectively. The disagreement in the area can also be due to the different time stamps between satellite image coverage and model simulation.

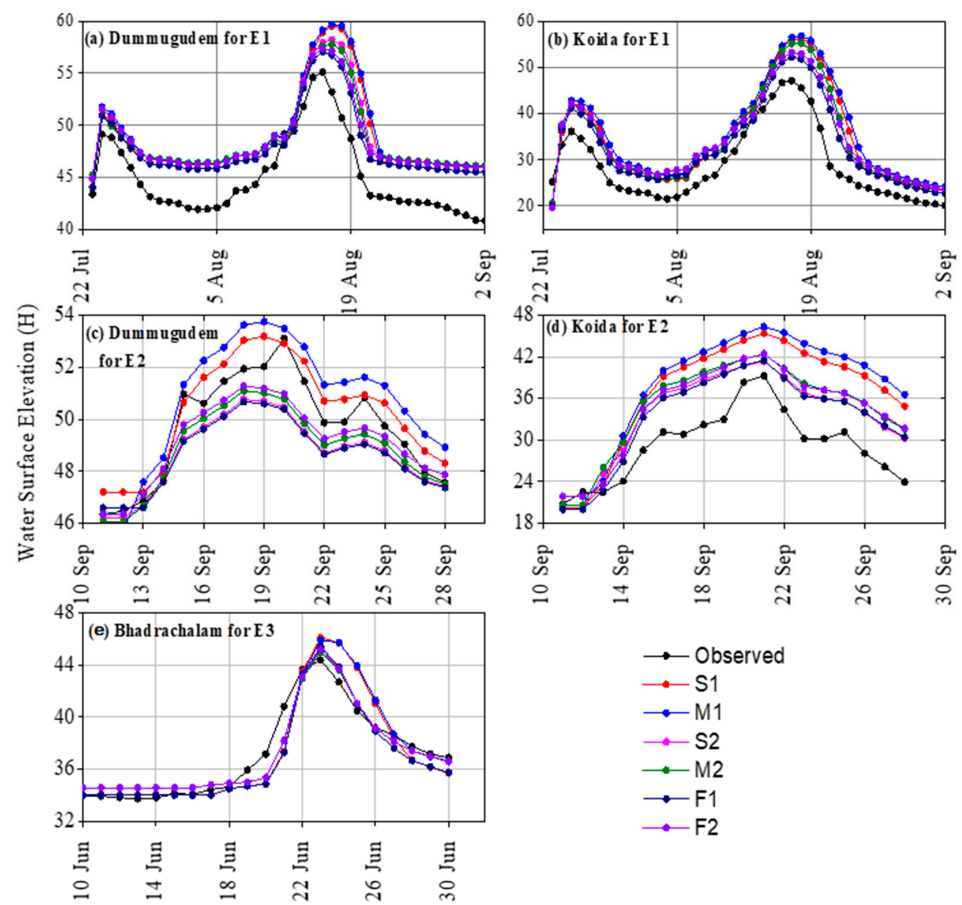


**Figure 8.** Time series plots of observed and simulated stage hydrographs at selected gauge stations from SRTM -30 m and MERIT-90 m. Plots (a,c) correspond to Dummgudem, (b,d) at Koida for E1 and E2 respectively. Plot (e) at Bhadrachalam for E3.

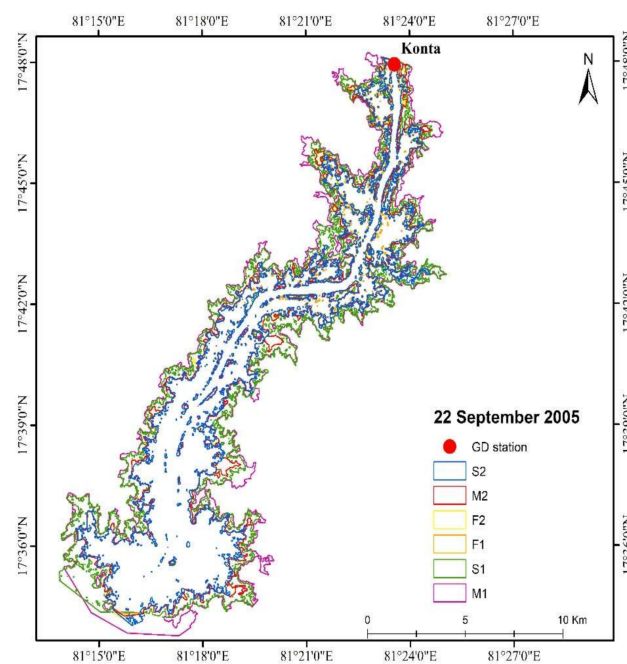


**Figure 9.** Ensemble of flood inundation regions using the six scenarios for the Sabari River on 22 September 2005 for the event E2.

### 3.6. Model Performance

The model performance analyzed by calculating various performance metrics for all six different scenarios for two locations, i.e., Dummugudem and Koida, for events E1 and E2, and Bhadrachalam for event E3 (Tables 3–5).

**Table 3.** Model performance metrics estimated by comparing simulated and observed water surface elevation (H) values for the events E1 with six scenarios. The results are presented for the upstream location—Dummugudem—and the downstream location—Koida.

Metric	E1											
	Dummugudem						Koida					
	S1	S2	M1	M2	F1	F2	S1	S2	M1	M2	F1	F2
r	0.88	0.92	0.89	0.97	0.95	0.95	0.93	0.95	0.92	0.95	0.96	0.95
KGE	0.81	0.88	0.82	0.85	0.85	0.85	0.64	0.7	0.63	0.7	0.82	0.77
d	0.79	0.79	0.77	0.74	0.84	0.81	0.86	0.88	0.83	0.88	0.92	0.88
MAE	3.58	3.69	4.06	2.96	2.99	3.49	6.02	5.59	7.07	5.57	4.37	5.64
RMSE	4.07	3.95	4.5	3.25	3.2	3.67	7.11	6.33	8.08	6.32	4.81	6.11
PBIAS	7.8	8.2	9	5	6.5	7.7	87.6	77.9	99.4	77.8	59.1	75.2

**Table 4.** Model performance metrics estimated by comparing simulated and observed water surface elevation (H) values for the events E2 with six scenarios. The results are presented for the upstream location—Dummugudem—and downstream location—Koida.

Metric	E2											
	Dummugudem						Koida					
	S1	S2	M1	M2	F1	F2	S1	S2	M1	M2	F1	F2
R	0.98	0.98	0.97	0.98	0.98	0.97	0.88	0.92	0.87	0.91	0.93	0.93
KGE	0.98	0.7	0.79	0.77	0.66	0.74	0.39	0.7	0.33	0.66	0.68	0.68
D	0.97	0.89	0.93	0.93	0.87	0.95	0.68	0.83	0.64	0.78	0.85	0.79
MAE	0.69	0.99	1.16	0.79	1.04	0.64	7.91	4.76	8.86	5.71	4.37	5.29
RMSE	0.75	1.21	1.24	0.98	1.27	0.82	8.65	5.1	9.72	6.14	4.79	5.8
PBIAS	1.3	−2	2	−1.6	−2	−1	25.9	15	29.5	18.7	13.7	17.8

**Table 5.** Model performance metrics are estimated by comparing the simulated and observed water surface elevation (H) values for the event E3 with six scenarios. The results are presented for the upstream location—Bhadrachalam.

Metric	E3					
	Bhadrachalam					
	S1	S2	M1	M2	F1	F2
R	0.93	0.96	0.94	0.96	0.96	0.96
KGE	0.78	0.94	0.85	0.94	0.94	0.95
D	0.96	0.97	0.96	0.98	0.97	0.98
MAE	1.05	0.76	1.04	0.7	0.77	0.7
RMSE	1.53	1.12	1.42	0.89	1.13	0.9
PBIAS	−0.1	−1.2	1.1	0	−1.2	0

For event E1 and for location Dummugudem, both scenarios M2 and F1 exhibited relatively low error, and consequently, small error verification metrics. However, only the F1 scenario exhibited higher values of goodness of fit measures. The scenarios F1 and F2, where 50% of the peak flow of E1 was underestimated showed a similar performance to the other scenarios, where observed flow boundary conditions were used (S1 to M2). This suggesting that the model structure is unable to simulate the stages obtained from the estimated flow boundary conditions. In addition, the estimated flow boundary conditions

used for E2 and E3 are in better agreement with the observed flows (Table 1). For event E2, all scenarios exhibited similar performance; however, S1 configuration exhibited lower error verification metrics. For both events E1 and E2, and for location Koida, F1 exhibited better performance among all in terms of error and goodness of fit measures. In addition, relatively increased error, and consequently, high values of error verification metrics, were observed for Koida. In general, configuration M1 exhibited higher error verification metrics, and better performance was observed for the configuration that used optimal Manning's  $n$  values. For event E3 and for location Bhadrachalam, all scenarios exhibited a similar performance, and scenarios M2 and F2 exhibited slightly smaller error verification metrics. In general, simulations of the event E3 at the Bhadrachalam exhibited better performance as compared to the events E1 and E2 at two other locations; note that the event E3 has a relatively standard hydrograph without much variation.

### 3.7. Event Hydrodynamics

To understand the role of model structure in the simulation of the water surface elevation, the model used the FME and DWE for two scenarios, i.e., S2 and M2. The two scenarios, S2 and M2, consist of optimized Manning's  $n$  values and observed flow boundary conditions in combination with the two DEM sources. Estimated hydrographs from two different model structures were compared at six locations that were randomly chosen on the main course of the Godavari River starting from upstream to downstream as well as at three GD locations that were mentioned earlier; six locations, i.e., L1, L2, L3, L4, L5 and L6, are shown in Figure 10. Three locations, L1, L2 and L3, are on the upstream of the river junction, and the remaining three locations are on the downstream of the river junction. Figure 10 has stage hydrographs for six locations and for three events, i.e., a total 18 plots. Each plot has four stage hydrographs and each set of two scenarios corresponds to simulations generated from FME and DWE. The plots suggest the following: (i) simulations from each set of the scenarios are of similar values for most of the locations for all events. Thus, no significant role of DEM is found except for location L1 for event E1 and locations L1 and L2 for event E2; (ii) for the event E1, the simulations derived from the DWE are relatively high for the downstream locations, whereas the simulations from the FME are relatively high for the upstream locations; (iii) for the events E2 and E3 and for all the locations, the simulations from FME obtain high values as compared to the simulations from DWE. Thus, the results suggest the importance of the model structure FME vs. DWE and the source of DEM for a few locations.

Furthermore, the estimated stage hydrographs based on FME and DWE were compared with the observed stage hydrograph at Dummugudem and Konda (for E1 and E2) and Bhadrachalam (for E3) GD stations (Figure 11). For the event E1 and for both locations, peak stage values were overestimated by two scenarios, i.e., DWE and MERIT-90 m and FME and SRTM-30 m, and underestimated by the other two scenarios. However, the estimated stage hydrographs are realistic for location Koida. For the event E2 and for the location Dummugudem, over- and underestimated stage hydrographs were observed for models runs of DWE and FME, respectively, whereas for location Koida, estimated stage hydrographs of all locations are overestimated. For the event E3 and for location Bhadrachalam, stages based on FME closely match with the observed values, and the remaining locations underestimated stages. The performance of the simulations varies with each event and scenarios as well indicating no systematic influence of model structure and DEM source. Additionally, note that these results differ with the results of the comparison of the streamflows at six locations along the main river, i.e., the estimated stage values are of higher values for the model run with FME for many locations for the event E2, and the opposite was observed for the location Koida for E2. Thus, the findings highlight the differences in FME- and DWE-derived estimates and hint at a detailed study.

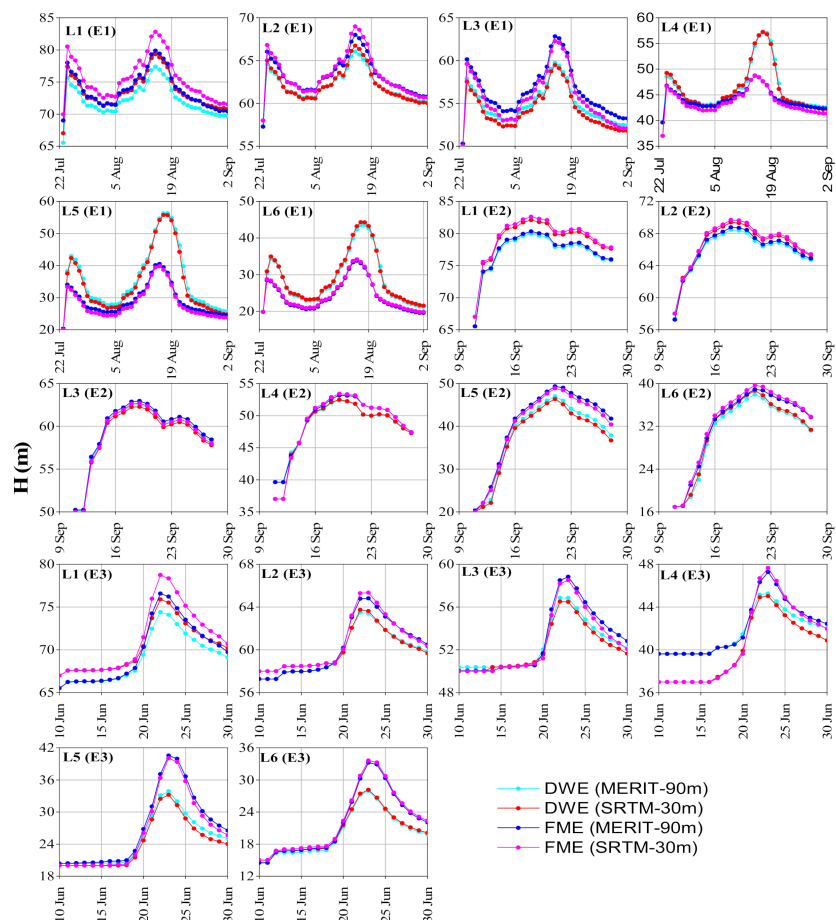


**Figure 10.** Comparison of the stage hydrographs obtained at six locations (L1 to L6) that are simulated from DWE and STRM-90 and SRTM-30 m DEMs. The event name corresponds to the location is mentioned right side.

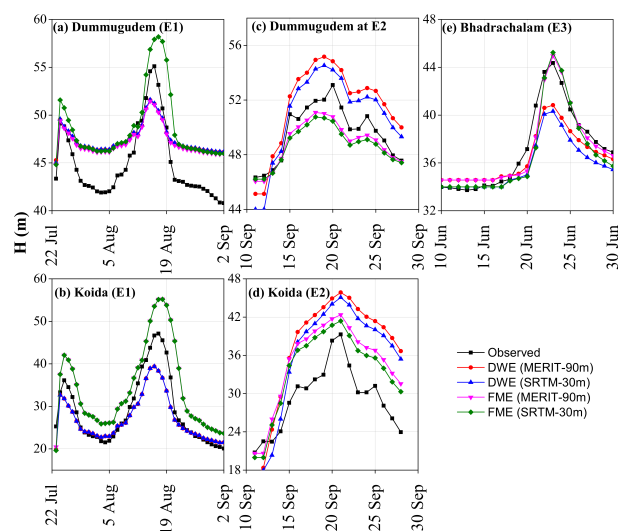


**Figure 11.** Stage hydrographs computed from the simulations when DWE and FME are used with SRTM-30 m and MERIT-90 m DEM. Comparison of the estimated stage hydrographs with observed values at GD stations for E1, E2 and E3. The figures, (a,b) are correspond to Dummugudem and Koida, respectively for event E1. The figures, (c,d) are correspond to Dummugudem and Koida, respectively E2, and the figure (e) corresponds to Bhadrachalam for event E3.

### 3.8. Insights on the Uncertainty

The HEC-RAS 2D model has no direct uncertainty estimation feature, and this study attempts to calculate the uncertainty in the model output considering different input sources of uncertainty as well as model structure. The two different DEMs, two sets of Manning's  $n$  and boundary conditions consist of both observed and estimated flows resulted six different scenarios, whereas the model structure varied treating the conservation of momentum based on either FME or DWE. In this section, we comment on these different sources.

While the SRTM-30 m DEM exhibited a relatively high  $H_{\text{Error}}$  as compared to the  $H_{\text{Error}}$  from MERIT-90 m DEM, it is interesting to know that these two DEMs exhibited a value of  $H_{\text{Error}}$   $<0.1$ ,  $<0.25$ ,  $<0.5$  and  $>0.5$  m for 85, 95, 99.8 and 0.2 percentage of the HEC-RAS 2D computational grid cells. While the difference is not significant for most of the cells, it is to be understood that the time stamp associated with the DEM also plays a role; for example, the DEMs may not be representative for the year 1986, as these DEMs and the surveyed cross-section profiles correspond to post-major flood event in 1986. A comparison of the DEMs with the measured values also showed the difference; however, instrument-based uncertainty should not be ignored, i.e., the measurements taken in the river course might be affected by the boat movement, which is not in the desired line relative to the point on the river bank. In addition, constant erosion, sediment deposition and changes in the morphology affect the DEM accuracy, and consequently, the calculations.

The scenarios with optimized Manning's  $n$  values yield stages of low error as compared to the values that read from the NLCD database, which has values as per the LULC category. This observation suggests that the land use category might not be truly representative in terms of either spatial resolution or, importantly, in terms of temporal dimension. Note that the LULC maps of a spatial resolution 100, 100 and 56 m correspond to the years 1985, 2005 and 2011 used for three events, 1986, 2005 and 2015, respectively. In addition, the season also play a role; for example, the river stream in the LULC map of 2005 (for E2) is invisible, which might be due to the data acquisition done in the dry period. This resulted in considering the high roughness values instead of lower values, which remained same even after optimization. Additionally, the uncertainty associated with Manning's  $n$  value for a land use or land cover class, i.e., multiple values or ranges, brings additional uncertainty, particularly in the modeling of extreme events. Estimated stages using Manning's  $n$  based on the NLCD data set are of high values for events E1 and E3, whereas the estimated values are in decent agreement with observed stage values for event E2.

Using of either observed or estimated streamflows at Konta on the Sabari River, which is one of the flow boundary conditions, resulted in different scenarios. The model performance in terms of goodness of fit and error metrics suggests the following: (i) relatively, there is a large influence of flows from the main river as compared to the tributary; (ii) there are changes in the velocity with respect to the time and along the channel; the rise in  $H$  in the downstream indicates that the increased turbulence is the velocity head added to any downstream change in bed level; (iii) large values of  $H$  influenced by rainfall event type, downstream hydraulic structures and river junction.

In addition to the above, uncertainties in estimates of various model parameters need to be explored systematically. These parameters are energy gradient line (EGL) slope, eddy viscosity transverse mixing coefficient ( $D$ ), implicit weighing factor ( $\theta$ ) and water surface tolerance parameter. The EGL slope can be computed with much less data. The EGL slope and  $D$  were explored for optimized values in the trial-and-error mode, but no significant change in the simulations were found. These two parameters are responsible for the velocity or energy head losses; however, the no significant effect suggests a systematic approach to explore the role of the parameters. In addition, convergence of the solution at the Courant number 2 when the error in cells is greater than the prescribed tolerance (0.003 m) impacts the analysis of error.

Similar estimated stages for the two scenarios of a model structure in combination with differences in the estimated stage values correspond to two different model structures, which emphasizes the role of local and convective acceleration terms. The simulated  $H$

values when DWE was used for the event E1 showed high peak flow values (>10 m) compared to the simulations using FME at L4 to L6 (Figure 10). This clearly highlights the role of the acceleration terms in simulating stage values. Furthermore, for locations L4 to L6, downstream of the river junction, which have relatively gentle river meanders, exhibited relatively high H values when modeled with DWE; local and convective acceleration terms were ignored. It is interesting to note that the DEM source dominated these terms for the event E2. The estimated H reflects hydrodynamics at six random locations as well as at GD locations, and suggest an increased error at Koida (downstream) as compared to Dummugudem (upstream).

#### 4. Discussion

It was observed that the flood inundation in the Lower Godavari Basin (LGB) is a function of the event magnitude and topographic aspects, such as elevation and roughness. Changes in the geometric aspects of river, for example contraction and expansion of the river, river meandering as well as river junction, play a significant role in the simulation of water surface elevation (H). In addition, the model structure that calculates the flow aspects also has a significant influence on the model output (stage values). A comparison of cross-sections also shows that DEM-based values are significantly missing. Cross-section profile suggests the following: (i) elevation values from two different DEMs are missing for a few locations; (ii) disagreement among the elevation values estimated from DEM sources and the measured values; (iii) large variations in the elevation values in the SRTM-30 m DEM.

A comparison of stage hydrographs from six scenarios indicates the high error for the event E1, which is the largest flood event, and the high error can be attributed to not providing the event rainfall and lack of detailed hydrodynamics. The median of  $H_{\text{Error}}$  is more for the event E3, which can be due to the land use and elevation changes, causing changes in Manning's n values. Furthermore, for event E3, H values estimated from FME are higher compared to DWE. The estimated values of H for E2 showed the differences with respect to the elevation models (Figure 11). The error in the estimation of H is higher in the downstream location. The uncertainty can be attributed to the failure of capturing the detailed hydrodynamics for the flood events that resulted from heavy rainfall (e.g., 206.13 mm for E1, 395.46 for E2 and 359.88 mm for E3 in the Sabari sub-basin), and higher streamflow upstream (20,000 m<sup>3</sup>/s to 60,000 m<sup>3</sup>/s in the Godavari River and 9000 m<sup>3</sup>/s to 20,000 m<sup>3</sup>/s in the Sabari River). The error in the H values is influenced by the mixing at the river junction as well as its energy-based junction method used in HEC-RAS 2D. Currently, the model assumes a 1D subcritical flow; however, parameters such as the angle of junction, zone of separation and flow ratio between the main and tributary are not considered. The river junction has its own role that needs to be explored [90–94].

The calibration of three parameters ( $\theta$ ,  $\Delta T$  and Manning's roughness coefficient) showed an overall improvement in the estimation of H through six scenarios. The calibration of  $\theta$  for the suggested range (0.6 to 1) for computational cells (error for the cells > tolerance error) exhibited values of error exceeding 1 m. Optimization of  $\Delta T$  for three events helped in estimating the consistent wave velocity. For the two events (E1 and E3), the optimized Manning's n values showed a greater sensitivity due to the land use change and the uncertainty from the data source and resolution. The LULC data were obtained at different resolutions from two sources (see Section 2.3.2) and the downscaling or aggregation of the data to the DEM's resolution caused a mismatch of land characteristics. Manning's n values from the different sources for the same land use or land cover feature were different; thus, the choice of roughness values and their optimization was also considered as one of the sources of uncertainty.

#### 5. Conclusions

In this study, a two-dimensional flood inundation modeling using HEC-RAS 2D was performed for six different scenarios that formed based on different sources of error in the model output. The study was carried out for a stretch of the Godavari River from Perur to

Polavaram and a stretch of the Sabari River, from Konta, which is the outlet of the Sabari River Basin, to Kunavaram, where the Sabari River meets the Godavari River. The model ran in unsteady mode for the selected three floods events, namely E1, E2 and E3, observed in three different years, namely 1986, 2005 and 2015, respectively. The model output, i.e., water surface elevation was analyzed for six scenarios for the three events, for selected locations. The configuration with SRTM-30 m DEM and Manning's  $n$  from NLCD data set yielded high error values and the scenarios that used optimized Manning's  $n$  values yielded small errors (E1 and E3). However, all scenarios exhibited a similar performance for event E3 at Bhadrachalam, and the estimated values of the event E3 are in better agreement with the observed stage values as compared to the events E1 and E2. Between the two events, E1 and E2, the estimated values for event E2 are in better agreement with the observed values; moreover, note that the event E1 is the largest event that was observed over the 50-year period of the record. The low performance of event E1 can be attributed to the uncertainty in the DEM, consequently land use classification or corresponding Manning's  $n$  values. In addition, the model ran for two different model structures developed using either the full momentum equation or the diffusion wave equation. The estimated values highlighted the differences between the two model structures, i.e., the model that used FME generated relatively high values for events E1 and E3 for the locations along the main course of the Godavari River. However, the opposite was observed for E2 at the GD location Koida.

The study allows to understand the role of the different input sources and model structures on the model output. This study recommends the following: (i) identification of a DEM that more accurately represents the river geometry; (ii) optimization of Manning's  $n$  values to reflect the LULC; (iii) analysis of the model with different model structures. While definite conclusions were drawn, a few questions remain to be answered, for example, the different influence of the model structure on the estimated stages at randomly selected locations and GD locations for events E1 and E2; role of the events in the context of varying flow magnitude and initial conditions. In addition, it is a known fact that the river junction plays a significant role, and its role in terms of mixing of flows, turbulence and backwater effects vary with various aspects of the flood event. In this context, the future work may include the following, i.e., increasing the sample of flood events, accounting for various hydraulic aspects such as the eddy viscosity and EGL slope, addressing the backwater effect in the Sabari tributary and separate the modeling of the river stretches before and after the river junction. In addition, combining the model output that is derived from multiple models, for example, LISFLOOD-FP and MIKE is recommended so that uncertainty in the model output will be accounted. In this context, this study provides insights on modeling uncertainties, with the key initiative to develop an ensemble flood inundation modeling for the study area.

**Author Contributions:** Conceptualization, V.C.S.; methodology, V.C.S.; software, V.C.S.; validation, S.R.; formal analysis, V.C.S. and S.R.; investigation, S.R.; resources, S.R.; data curation, V.C.S.; writing—original draft preparation, V.C.S.; writing—review and editing, S.R.; visualization, V.C.S.; supervision, S.R.; project administration, S.R. All authors have read and agreed to the published version of the manuscript.

**Funding:** This research was funded by the Ministry of Human Resources Development (MHRD) of India at the Indian Institute of Technology Hyderabad.

**Institutional Review Board Statement:** Not applicable.

**Informed Consent Statement:** Not applicable.

**Data Availability Statement:** Rainfall and flow data can be obtained from the Central Water Commission (CWC) and India Meteorological Department (IMD), respectively. Land use and land cover data for 2011 can be ordered from ISRO-Bhuvan website. The remaining data that is mentioned in the Section 2.2 is available online.

**Acknowledgments:** The authors like to acknowledge Ranga Reddi, Raghu Ram and Murali Mohan, Krishna and Godavari Basin Organization (KGB), CWC for providing streamflow data and other basin related information. Additionally, the authors express their gratitude to the India Meteorological Department (IMD) for providing the daily gridded rainfall data for this study.

**Conflicts of Interest:** The authors declare no conflict of interest.

## References

- Hooke, J.M.; Mant, J.M. Geomorphological impacts of a flood event on ephemeral channels in SE Spain. *Geomorphology* **2000**, *34*, 163–180. [[CrossRef](#)]
- Costabile, P.; Costanzo, C.; Ferraro, D.; Macchione, F.; Petaccia, G. Performances of the new HEC-RAS version 5 for 2-D hydrodynamic-based rainfall-runoff simulations at basin scale: Comparison with a state-of-the-art model. *Water* **2020**, *12*, 2326. [[CrossRef](#)]
- Pender, G.; Néelz, S. Use of computer models of flood inundation to facilitate communication in flood risk management. *Environ. Hazards* **2007**, *7*, 106–114. [[CrossRef](#)]
- Rampinelli, C.G.; Knack, I.; Smith, T. Flood mapping uncertainty from a restoration perspective: A practical case study. *Water* **2020**, *12*, 1948. [[CrossRef](#)]
- Bates, P.D.; Pappenberger, F.; Romanowicz, R.J. Uncertainty in flood inundation modelling. In *Applied Uncertainty Analysis for Flood Risk Management*; Imperial College Press: London, UK, 2014.
- Pappenberger, F.; Beven, K.; Horritt, M.; Blazkova, S. Uncertainty in the calibration of effective roughness parameters in HEC-RAS using inundation and downstream level observations. *J. Hydrol.* **2005**, *302*, 46–69. [[CrossRef](#)]
- Willis, T.; Wright, N.; Sleight, A. Systematic analysis of uncertainty in 2D flood inundation models. *Environ. Model. Softw.* **2019**, *122*. [[CrossRef](#)]
- Teng, J.; Jakeman, A.J.; Vaze, J.; Croke, B.F.W.; Dutta, D.; Kim, S. Flood inundation modelling: A review of methods, recent advances and uncertainty analysis. *Environ. Model. Softw.* **2017**, *90*, 201–216. [[CrossRef](#)]
- Merwade, V.; Olivera, F.; Arabi, M.; Edleman, S. Uncertainty in flood inundation mapping: Current issues and future directions. *J. Hydrol. Eng.* **2008**, *13*, 608–620. [[CrossRef](#)]
- Liu, Z.; Merwade, V.; Jafarzaghan, K. Investigating the role of model structure and surface roughness in generating flood inundation extents using one- and two-dimensional hydraulic models. *J. Flood Risk Manag.* **2019**, *12*, e12347. [[CrossRef](#)]
- Cook, A.; Merwade, V. Effect of topographic data, geometric configuration and modeling approach on flood inundation mapping. *J. Hydrol.* **2009**, *377*, 131–142. [[CrossRef](#)]
- Liu, Z.; Merwade, V. Accounting for model structure, parameter and input forcing uncertainty in flood inundation modeling using Bayesian model averaging. *J. Hydrol.* **2018**, *565*, 138–149. [[CrossRef](#)]
- Todini, E. Predictive uncertainty assessment in real time flood forecasting: Part of NATO Science for Peace and Security Series. In *Uncertainties in Environmental Modelling and Consequences for Policy Making*; Springer: Dordrecht, The Netherlands, 2009; pp. 205–228. [[CrossRef](#)]
- Aghakouchak, A.; Nakhjiri, N.; Habib, E. An educational model for ensemble streamflow simulation and uncertainty analysis. *Hydrol. Earth Syst. Sci.* **2013**, *17*, 445–452. [[CrossRef](#)]
- Harrigan, S.; Prudhomme, C.; Parry, S.; Smith, K.; Tanguy, M. Benchmarking ensemble streamflow prediction skill in the UK. *Hydrol. Earth Syst. Sci.* **2018**, *22*, 2023–2039. [[CrossRef](#)]
- Schick, S.; Rössler, O.; Weingartner, R. Monthly streamflow forecasting at varying spatial scales in the Rhine basin. *Hydrol. Earth Syst. Sci.* **2018**, *22*, 929–942. [[CrossRef](#)]
- Demeritt, D.; Nobert, S.; Cloke, H.L.; Pappenberger, F. The European Flood Alert System and the communication, perception, and use of ensemble predictions for operational flood risk management. *Hydrol. Process.* **2013**, *27*, 147–157. [[CrossRef](#)]
- Alfieri, L.; Pappenberger, F.; Wetterhall, F.; Haiden, T.; Richardson, D.; Salamon, P. Evaluation of ensemble streamflow predictions in Europe. *J. Hydrol.* **2014**, *517*, 913–922. [[CrossRef](#)]
- Bischiotti, K.; van den Hurk, B.; Zsoter, E.; Coughlan de Perez, E.; Grillakis, M.; Aerts, J.C.J.H. Evaluation of a global ensemble flood prediction system in Peru. *Hydrol. Sci. J.* **2019**, *64*, 1171–1189. [[CrossRef](#)]
- Fleischmann, A.S.; Paiva, R.C.D.; Collischonn, W.; Siqueira, V.A.; Paris, A.; Moreira, D.M.; Papa, F.; Bitar, A.A.; Parrens, M.; Aires, F.; et al. Trade-Offs Between 1-D and 2-D Regional River Hydrodynamic Models. *Water Resour. Res.* **2020**, *56*. [[CrossRef](#)]
- Néelz, S.; Pender, G. *Desktop Review of 2D Hydraulic Modelling Packages*; Environment Agency: Bristol, UK, 2009.
- Bates, P.D.; De Roo, A.P.J. A simple raster-based model for flood inundation simulation. *J. Hydrol.* **2000**, *236*, 54–77. [[CrossRef](#)]
- Patro, S.; Chatterjee, C.; Mohanty, S.; Singh, R.; Raghuwanshi, N.S. Flood inundation modeling using MIKE FLOOD and remote sensing data. *J. Indian Soc. Remote Sens.* **2009**, *37*, 107–118. [[CrossRef](#)]
- Sampson, C.C.; Smith, A.M.; Bates, P.B.; Neal, J.C.; Alfieri, L.; Freer, J.E. A high-resolution global flood hazard model. *Water Resour. Res.* **2015**, *51*, 7358–7381. [[CrossRef](#)] [[PubMed](#)]
- Yamazaki, D.; Kanae, S.; Kim, H.; Oki, T. A physically based description of floodplain inundation dynamics in a global river routing model. *Water Resour. Res.* **2011**, *47*. [[CrossRef](#)]
- Schumann, G.J.P.; Neal, J.C.; Voisin, N.; Andreadis, K.M.; Pappenberger, F.; Phanthuwongpakdee, N.; Hall, A.C.; Bates, P.D. A first large-scale flood inundation forecasting model. *Water Resour. Res.* **2013**, *49*, 6248–6257. [[CrossRef](#)]

27. Abily, M.; Bertrand, N.; Delestre, O.; Gourbesville, P.; Duluc, C.-M. Spatial Global Sensitivity Analysis of High Resolution classified topographic data use in 2D urban flood modelling. *Environ. Model. Softw.* **2016**, *77*, 183–195. [[CrossRef](#)]
28. Baugh, C.A.; Bates, P.D.; Schumann, G.; Trigg, M.A. SRTM vegetation removal and hydrodynamic modeling accuracy. *Water Resour. Res.* **2013**, *49*, 5276–5289. [[CrossRef](#)]
29. Pappenberger, F.; Matgen, P.; Beven, K.J.; Henry, J.B.; Pfister, L.; Fraipont, P. Influence of uncertain boundary conditions and model structure on flood inundation predictions. *Adv. Water Resour.* **2006**, *29*, 1430–1449. [[CrossRef](#)]
30. Sampson, C.C.; Bates, P.D.; Neal, J.C.; Horritt, M.S. An automated routing methodology to enable direct rainfall in high resolution shallow water models. *Hydrol. Process.* **2013**, *27*, 467–476. [[CrossRef](#)]
31. Sanders, B.F. Evaluation of on-line DEMs for flood inundation modeling. *Adv. Water Resour.* **2007**, *30*, 1831–1843. [[CrossRef](#)]
32. Casas, A.; Benito, G.; Thorndycraft, V.R.; Rico, M. The topographic data source of digital terrain models as a key element in the accuracy of hydraulic flood modelling. *Earth Surf. Process. Landf.* **2006**, *31*, 444–456. [[CrossRef](#)]
33. Saksena, S.; Merwade, V. Incorporating the Effect of DEM Resolution and Accuracy for Improved Flood Inundation Mapping Integrated Flood Modeling for Improved Understanding of River-Floodplain Hydrodynamics View project Prediction in data-scarce regions: Regionalization and catchment classification from a general perspective View project Incorporating the effect of DEM resolution and accuracy for improved flood inundation mapping. *Artic. J. Hydrol.* **2015**, *530*. [[CrossRef](#)]
34. Prakash Mohanty, M.; Nithya, S.; Nair, A.S.; Indu, J.; Ghosh, S.; Mohan Bhatt, C.; Srinivasa Rao, G.; Karmakar, S. Sensitivity of various topographic data in flood management: Implications on inundation mapping over large data-scarce regions. *J. Hydrol.* **2020**, *590*, 125523. [[CrossRef](#)]
35. Yan, K.; Di Baldassarre, G.; Solomatine, D.P. Exploring the potential of SRTM topographic data for flood inundation modelling under uncertainty. *J. Hydroinf.* **2013**, *15*. [[CrossRef](#)]
36. Haque, M.M.; Seidou, O.; Mohammadian, A.; Gado Djibo, A. Development of a time-varying MODIS/2D hydrodynamic model relationship between water levels and flooded areas in the Inner Niger Delta, Mali, West Africa. *J. Hydrol. Reg. Stud.* **2020**, *30*. [[CrossRef](#)]
37. Bates, P.D.; Horritt, M.S.; Aronica, G.; Beven, K. Bayesian updating of flood inundation likelihoods conditioned on flood extent data. *Hydrol. Process.* **2004**, *18*, 3347–3370. [[CrossRef](#)]
38. Bates, P.D.; Horritt, M.S.; Fewtrell, T.J. A simple inertial formulation of the shallow water equations for efficient two-dimensional flood inundation modelling. *J. Hydrol.* **2010**, *387*, 33–45. [[CrossRef](#)]
39. Romanowicz, R.; Beven, K. Estimation of flood inundation probabilities as conditioned on event inundation maps. *Water Resour. Res.* **2003**, *39*. [[CrossRef](#)]
40. Apel, H.; Aronica, G.T.; Kreibich, H.; Thielen, A.H. Flood risk analyses—How detailed do we need to be? *Nat. Hazards* **2009**, *49*, 79–98. [[CrossRef](#)]
41. De Almeida, G.A.M.; Bates, P. Applicability of the local inertial approximation of the shallow water equations to flood modeling. *Water Resour. Res.* **2013**, *49*, 4833–4844. [[CrossRef](#)]
42. Loi, N.K.; Liem, N.D.; Tu, L.H.; Hong, N.T.; Truong, C.D.; Tram, V.N.Q.; Nhat, T.T.; Anh, T.N.; Jeong, J. Automated procedure of real-time flood forecasting in Vu Gia—Thu Bon river basin, Vietnam by integrating SWAT and HEC-RAS models. *J. Water Clim. Chang.* **2019**, *10*, 535–545. [[CrossRef](#)]
43. Ferguson, C.; Fenner, R. The impact of Natural Flood Management on the performance of surface drainage systems: A case study in the Calder Valley. *J. Hydrol.* **2020**, *590*, 125354. [[CrossRef](#)]
44. Doong, D.J.; Lo, W.; Vojinovic, Z.; Lee, W.L.; Lee, S.P. Development of a new generation of flood inundation maps—A case study of the coastal city of Tainan, Taiwan. *Water* **2016**, *8*, 521. [[CrossRef](#)]
45. Patel, D.P.; Ramirez, J.A.; Srivastava, P.K.; Bray, M.; Han, D. Assessment of flood inundation mapping of Surat city by coupled 1D/2D hydrodynamic modeling: A case application of the new HEC-RAS 5. *Nat. Hazards* **2017**, *89*, 93–130. [[CrossRef](#)]
46. Horritt, M.S.; Bates, P.D. Evaluation of 1D and 2D numerical models for predicting river flood inundation. *J. Hydrol.* **2002**, *268*, 87–99. [[CrossRef](#)]
47. Rahimzadeh, O.; Bahremand, A.; Noura, N.; Mukolwe, M. Evaluating flood extent mapping of two hydraulic models, 1D HEC-RAS and 2D LISFLOOD-FP in comparison with aerial imagery observations in Gorgan flood plain, Iran. *Nat. Resour. Model.* **2019**, *32*, e12214. [[CrossRef](#)]
48. Shustikova, I.; Domeneghetti, A.; Neal, J.C.; Bates, P.; Castellarin, A. Comparing 2D capabilities of HEC-RAS and LISFLOOD-FP on complex topography. *Hydrol. Sci. J.* **2019**, *64*, 1769–1782. [[CrossRef](#)]
49. Neelz, S.; Pender, G. *Benchmarking the Latest Generation of 2D Hydraulic Modelling Packages*; Environment Agency: Bristol, UK, 2013.
50. Hunter, N.M.; Bates, P.D.; Neelz, S.; Pender, G.; Villanueva, I.; Wright, N.G.; Liang, D.; Falconer, R.A.; Lin, B.; Waller, S.; et al. Benchmarking 2D hydraulic models for urban flooding. *Proc. Inst. Civ. Eng. Water Manag.* **2008**, *161*, 13–30. [[CrossRef](#)]
51. Roberts, S.; Nielsen, O.; Gray, D.; Sexton, J. *ANUGA User Manual*; Geoscience Australia: Symonston, ACT, Australia, 2015.
52. Savage, J.T.S.; Bates, P.; Freer, J.; Neal, J.; Aronica, G. When does spatial resolution become spurious in probabilistic flood inundation predictions? *Hydrol. Process.* **2016**, *30*, 2014–2032. [[CrossRef](#)]
53. Jafarzadegan, K.; Merwade, V. A DEM-based approach for large-scale floodplain mapping in ungauged watersheds. *J. Hydrol.* **2017**, *550*, 650–662. [[CrossRef](#)]
54. Yamazaki, D.; Baugh, C.A.; Bates, P.D.; Kanae, S.; Alsdorf, D.E.; Oki, T. Adjustment of a spaceborne DEM for use in floodplain hydrodynamic modeling. *J. Hydrol.* **2012**, *436–437*, 81–91. [[CrossRef](#)]

55. Medeiros, S.C.; Hagen, S.C.; Weishampel, J.F. Comparison of floodplain surface roughness parameters derived from land cover data and field measurements. *J. Hydrol.* **2012**, *452–453*, 139–149. [[CrossRef](#)]
56. Dimitriadis, P.; Tegos, A.; Oikonomou, A.; Pagana, V.; Koukouvinos, A.; Mamassis, N.; Koutsoyiannis, D.; Efstratiadis, A. Comparative evaluation of 1D and quasi-2D hydraulic models based on benchmark and real-world applications for uncertainty assessment in flood mapping. *J. Hydrol.* **2016**, *534*, 478–492. [[CrossRef](#)]
57. Vatanchi, S.M.; Maghrebi, M.F. Uncertainty in Rating-Curves Due to Manning Roughness Coefficient. *Water Resour. Manag.* **2019**, *33*, 5153–5167. [[CrossRef](#)]
58. Bellos, V.; Kourtis, I.M.; Moreno-Rodenas, A.; Tsihrintzis, V.A. Quantifying roughness coefficient uncertainty in urban flooding simulations through a simplified methodology. *Water* **2017**, *9*, 944. [[CrossRef](#)]
59. Ozdemir, H.; Sampson, C.C.; De Almeida, G.A.M.; Bates, P.D. Evaluating scale and roughness effects in urban flood modelling using terrestrial LIDAR data. *Hydrol. Earth Syst. Sci.* **2013**, *17*, 4015–4030. [[CrossRef](#)]
60. Huang, Y.; Qin, X. Uncertainty analysis for flood inundation modelling with a random floodplain roughness field. *Environ. Syst. Res.* **2014**, *3*, 9. [[CrossRef](#)]
61. Praskievicz, S.; Carter, S.; Dhondia, J.; Follum, M. Flood-inundation modeling in an operational context: Sensitivity to topographic resolution and Manning's n. *J. Hydroinf.* **2020**, *22*, 1338–1350. [[CrossRef](#)]
62. Fent, I.; Putti, M.; Gregoretti, C.; Lanzoni, S. Modeling shallow water flows on general terrains. *Adv. Water Resour.* **2018**, *121*, 316–332. [[CrossRef](#)]
63. Smart, G.M. Improving flood hazard prediction models. *Int. J. River Basin Manag.* **2018**, *16*, 449–456. [[CrossRef](#)]
64. Freer, J.; Beven, K.; Ambrose, B. Bayesian estimation of uncertainty in runoff prediction and the value of data: An application of the GLUE approach. *Water Resour. Res.* **1996**, *32*, 2161–2173. [[CrossRef](#)]
65. Hunter, N.M.; Bates, P.D.; Horritt, M.S.; de Roo, P.J.; Werner, M.G.F. Utility of different data types for calibrating flood inundation models within a GLUE framework. *Hydrol. Earth Syst. Sci.* **2005**, *9*, 412–430. [[CrossRef](#)]
66. Jung, Y.; Merwade, V. Uncertainty Quantification in Flood Inundation Mapping Using Generalized Likelihood Uncertainty Estimate and Sensitivity Analysis. *J. Hydrol. Eng.* **2012**, *17*, 507–520. [[CrossRef](#)]
67. Pappenberger, F.; Beven, K.J.; Ratto, M.; Matgen, P. Multi-method global sensitivity analysis of flood inundation models. *Adv. Water Resour.* **2008**, *31*, 1–14. [[CrossRef](#)]
68. Pappenberger, F.; Beven, K.J.; Hunter, N.M.; Bates, P.D.; Gouweleeuw, B.T.; Thielen, J.; de Roo, A.P.J. Cascading model uncertainty from medium range weather forecasts (10 days) through a rainfall-runoff model to flood inundation predictions within the European Flood Forecasting System (EFFS). *Hydrol. Earth Syst. Sci.* **2005**, *9*, 381–393. [[CrossRef](#)]
69. Di Mauro, C.; Hostache, R.; Matgen, P.; Pelich, R.; Chini, M.; van Leeuwen, P.J.; Nichols, N.; Blöschl, G. Assimilation of probabilistic flood maps from SAR data into a hydrologic-hydraulic forecasting model: A proof of concept. *Hydrol. Earth Syst. Sci.* **2020**, 1–24. [[CrossRef](#)]
70. De Luca, D.L.; Biondi, D. Bivariate return period for design hyetograph and relationship with T-year design flood peak. *Water* **2017**, *9*, 673. [[CrossRef](#)]
71. Yue, S.; Rasmussen, P. Bivariate frequency analysis: Discussion of some useful concepts in hydrological application. *Hydrol. Process.* **2002**, *16*, 2881–2898. [[CrossRef](#)]
72. Volpi, E.; Fiori, A. Design event selection in bivariate hydrological frequency analysis. *Hydrol. Sci. J.* **2012**, *57*, 1506–1515. [[CrossRef](#)]
73. Nelsen, R.B. *An Introduction to Copulas*; Springer: Berlin/Heidelberg, Germany, 1998. Available online: <https://www.springer.com/gp/book/9780387286594> (accessed on 5 January 2021).
74. Krishna and Godavari Basin Organization, KGBO. Available online: <http://cwc.gov.in/kgbo/home> (accessed on 5 November 2020).
75. Das, J.; Umamahesh, N.V. Downscaling Monsoon Rainfall over River Godavari Basin under Different Climate-Change Scenarios. *Water Resour. Manag.* **2016**, *30*, 5575–5587. [[CrossRef](#)]
76. Garg, S.; Mishra, V. Role of extreme precipitation and initial hydrologic conditions on floods in Godavari river basin, India. *Water Resour. Res.* **2019**, *55*. [[CrossRef](#)]
77. Raju, K.S.; Kumar, D.N. Impact of Climate Change on Water Resources With Modeling Techniques and Case Studies Introduction. In *Impact of Climate Change on Water Resources: With Modeling Techniques and Case Studies*; Springer: Berlin/Heidelberg, Germany, 2018; pp. 1–25.
78. Mujumdar, P.P.; Nagesh Kumar, D. *Floods in a Changing Climate: Hydrologic Modeling*; Cambridge University Press: Cambridge, UK, 2010.
79. Bhatt, C.M.; Rao, G.S.; Diwakar, P.G.; Dadhwal, V.K. Development of flood inundation extent libraries over a range of potential flood levels: A practical framework for quick flood response. *Geomat. Nat. Hazards Risk* **2017**, *8*, 384–401. [[CrossRef](#)]
80. Amarnath, C.R.; Thatikonda, S. Study on backwater effect due to Polavaram Dam Project under different return periods. *Water* **2020**, *12*, 576. [[CrossRef](#)]
81. Yamazaki, D.; Ikeshima, D.; Tawatari, R.; Yamaguchi, T.; O'Loughlin, F.; Neal, J.C.; Sampson, C.C.; Kanae, S.; Bates, P.D. A high-accuracy map of global terrain elevations. *Geophys. Res. Lett.* **2017**, *44*, 5844–5853. [[CrossRef](#)]
82. Farr, T.G.; Kobrick, M. Shuttle radar topography mission produces a wealth of data. *Eos* **2000**, *81*, 583–585. [[CrossRef](#)]
83. Bhuvan. Thematic Data Dissemination, Free GIS Data, OGC Services, Clip and Ship. Available online: <https://bhuvan-app1.nrsc.gov.in/thematic/thematic/index.php> (accessed on 5 November 2020).

84. McCuen, R.H. *Hydrologic Analysis and Design*; Prentice-Hall: Upper Saddle River, NJ, USA, 1998.
85. Brunner, G. *HEC-RAS River Analysis System, Hydraulic Reference Manual, Version 4.1*; Hydrologic Engineering Center: Davis, CA, USA, 2010.
86. Brunner, G.W. *HEC-RAS River Analysis System, 2D Modeling User's Manual Version 5.0*; Hydrologic Engineering Center: Davis, CA, USA, 2016.
87. De Moura, C.A.; Kubrusly, C.S. *The Courant–Friedrichs–Lewy (CFL) Condition*; Birkhäuser Boston: Cambridge, MA, USA, 2013.
88. Legates, D.R.; McCabe, G.J. Evaluating the use of “goodness-of-fit” measures in hydrologic and hydroclimatic model validation. *Water Resour. Res.* **1999**, *35*, 233–241. [[CrossRef](#)]
89. Gupta, H.V.; Kling, H.; Yilmaz, K.K.; Martinez, G.F. Decomposition of the mean squared error and NSE performance criteria: Implications for improving hydrological modelling. *J. Hydrol.* **2009**, *377*, 80–91. [[CrossRef](#)]
90. Ghostine, R.; Mose, R.; Vazquez, J.; Ghenaïm, A.; Grégoire, C. Two-Dimensional Simulation of Subcritical Flow at a Combining Junction: Luxury or Necessity? *J. Hydraul. Eng.* **2010**, *136*, 799–805. [[CrossRef](#)]
91. Ghostine, R.; Vazquez, J.; Terfous, A.; Mose, R.; Ghenaïm, A. Comparative study of 1D and 2D flow simulations at open-channel junctions. *J. Hydraul. Res.* **2012**, *50*, 164–170. [[CrossRef](#)]
92. Roy, A.G.; Woldenberg, M.J. A Model for Changes in Channel form at a River Confluence. *J. Geol.* **1986**, *94*, 402–411. [[CrossRef](#)]
93. Wang, X.; Yan, X.; Duan, H.; Liu, X.; Huang, E. Experimental study on the influence of river flow confluences on the open channel stage–discharge relationship. *Hydrol. Sci. J.* **2019**, *64*, 2025–2039. [[CrossRef](#)]
94. Roca, M.; Martín-Vide, J.P.; Moreta, P.J.M. Modelling a torrential event in a river confluence. *J. Hydrol.* **2009**, *364*, 207–215. [[CrossRef](#)]